Dyes and Pigments 124 (2016) 53–62

Contents lists available at ScienceDirect

Dyes and Pigments

journal homepage: www.elsevier.com/locate/dyepig

Conjugated dye-intercalated fluoromica hybrids displaying tunability of optical properties through packing variation

G. Leone [a], U. Giovanella [a], F. Galeotti [a], L. Barba [b], G. Arrighetti [b], G. Scavia [a], A. Rapallo [a], W. Porzio [a, *]

[a] Istituto per lo Studio delle Macromolecole del C.N.R., via E. Bassini 15, 20133 Milano, Italy
[b] Istituto di Cristallografia del C.N.R., Strada Statale 14-Km 163,5 Area Science Park, 34149 Basovizza, Trieste, Italy

ARTICLE INFO

Article history:
Received 17 July 2015
Received in revised form
4 September 2015
Accepted 6 September 2015
Available online 14 September 2015

Keywords:
Layered silicates
Conjugated dyes
Crystal packing
Photoluminescence
Modelling
Intercalation

ABSTRACT

Conjugated dye-intercalated fluoromica hybrids involving three different cationic organic dyes, i.e. oxazine, rhodamine and ter-fluorene derivatives, have been characterized by synchrotron X-ray diffraction (XRD) in combination with optical spectroscopy. The results show the tunability of the dye packing, hence of the absorption and emission properties, as a function of both type and amount of intercalated molecule. Suitable molecular models compatible with XRD findings, accounting for the observed optical behavior, are proposed and discussed.

1. Introduction

Hybrid composites constitute a milestone in the development of functional and structured materials displaying peculiar properties and improved performances. Typically, these assembled materials combine the intrinsic features of both organic and inorganic components, leading to enhanced mechanical, physical and thermal properties [1–3]. Among the hybrid composites, those comprising π-conjugated organic chromophores have gained considerable interest for the possibility of developing materials with specific optical and electronic properties [4–7]. In fact, over the decades scientists focused their efforts towards the synthesis of hybrid multifunctional assemblies for different optoelectronic applications such as waveguide laser cavities [8], optical memory systems [9], artificial antenna systems [10], and for the manufacturing of optical sensors [11] and light emitting diodes [12]. In these systems, the inorganic component is arranged into ordered nano-scale architectures embedding photofunctional organic π-conjugated dyes.

Among the inorganic nano-structured materials, layered silicates have been widely used as hosts owing to their ion-exchange capability, large specific surface area, and unique two-dimensional expandable intra-layer space [13,14]. These specific features enable the tuning of the interaction between the embedded organic dyes in a sandwich-type intercalation by surface chemistry (i.e., ion-exchange and grafting reactions).

Recently, we have synthesized different SOMASIF 100 (**SME**) hybrids based on an intercalated organic dye and a polymer matrix wrapping the inorganic nanostructure, and we have shown that the **SME** interlayer spacing can be varied by changing the type of intercalated dye and its loading [14–17]. The main goals achieved, besides the enhanced processability imparted by the polymer, are the improvement of the dye photo-, thermo-, and chemical-stability, and the control of the accommodation of the guest to realize efficient dye assemblies, thus allowing the tuning of the hybrid's photo-functions.

Because of the great interest for the applications of these polymer hybrids in optoelectronic devices [18], a deeper structural characterization of the crystalline dye-intercalated **SME** precursors is desirable. Quite recently three contributions concerning the complete crystal structure of hybrids constituted by layered silicate and organic molecules have been reported [19–21]; in these

* Corresponding author.
E-mail address: w.porzio@ismac.cnr.it (W. Porzio).

http://dx.doi.org/10.1016/j.dyepig.2015.09.003
0143-7208/

studies the molecules taken into consideration were either not conjugated or small, and no significant optoelectronic properties could be conceived.

In this work, aiming to gain a deeper insight into the dye arrangement within the interlayer spacing, the salts of three prototypal π-conjugated dyes appealing for optoelectronic applications, were studied by means of synchrotron XRD investigations. The chemical structure of three dyes differing in their size, shape, and stiffness are all shown in Scheme 1, i.e. oxazine-1 chloride (**Ox1**$^+$), rhodamine 6G chloride (**R6G**$^+$), and 2,7-bis(9,9-dioctylfluorene-2-yl)-9,9-bis[6-(trimethylammonium)hexyl]fluorene dibromide (**TF**$^{2+}$).

Moreover, suitable molecular models compatible with XRD findings are proposed and the agreement with the optical properties of the hybrids is discussed.

2. Experimental

2.1. Hybrid preparation

The materials were synthesized following the procedures developed for each specific case, detailed in Refs. [14], [16], and [17], for **Ox1**$^+$, **TF**$^{2+}$ and **R6G**$^+$, respectively. A general procedure however is reported in Supplementary data.

2.2. X-ray diffraction

Powders loaded into a sealed capillary were examined at 25 °C. GIWAXS measurements were performed at the X-ray diffraction beamline 5.2 at the Synchrotron Radiation Facility Elettra in Trieste (Italy). The X-ray beam emitted by the wiggler source on the Elettra 2 GeV electron storage ring was monochromatized by a Si(111) double crystal monochromator, focused on the sample and collimated by a double set of slits giving a spot size of 0.2 × 0.2 mm. The beam was monochromatized at energies from 6.2 keV to 10.34 keV ($1.2 \leq \lambda \leq 2$ nm) both for films and powders. Samples were oriented by means of a four-circle diffractometer with a motorized goniometric head. The X-ray beam direction was fixed, while the sample holder could be rotated about the different diffractometer axes, in order to reach the sample surface alignment in the horizontal plane containing the X-ray beam by means of laser light reflection. Subsequently it was possible to rotate it around an axis perpendicular to this plane or, alternatively, vary the angle between beam and surface (angle of incidence). Bidimensional diffraction patterns were recorded with a 2M Pilatus silicon pixel X-ray detector (DECTRIS Ltd., Baden, Switzerland) positioned perpendicularly to the incident beam, at 200 mm distance from the sample, to record the diffraction patterns in reflection geometry. Sample and detector were kept still during the measurements. The sample inclination to the beam was changed from $\omega = -0.05°$ to $\omega = 0.25°$, in steps of 0.05° yielding seven diffraction images. The q resolution of the 2D collected images was estimated by means of Lanthanum Hexaboride powder (NIST standard reference material 660a) and was evaluated ranging from 0.2 to 0.3 nm^{-1} both for q_z and q_{xy}, in agreement with other synchrotron measurements [22,23]. The same calibration standard allowed for the integration of 2D patterns using the software Fit2D [24] yielding powder-like patterns of intensity vs. diffraction angle, corrected for geometry, Lorentz, and beam polarization effects. Peaks positions were extracted by means of the program Winplotr [25]. Powders, when available in sufficient amount, were also examined using an Anton&Parr Camera under nitrogen flux and Siemens D-500 diffractometer (Cu Kα radiation, $\lambda = 0.154$ nm). The operating voltage and current were 40 kV and 40 mA, respectively. Data were collected from 3° to 33° 2θ at 0.05° 2θ intervals.

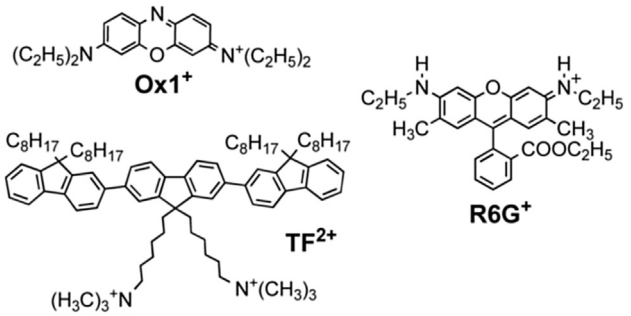

Scheme 1. The chemical structure of the organic dyes considered in the study.

2.3. Optical analysis

Due to the extremely low solubility of the hybrids, the optical characterization of the composite crystalline powders was performed on ground samples in KBr pressed pellets.

UV–visible absorption measurements were carried out via PerkinElmer Lambda900. The continuous wave photoluminescence (PL) spectra were recorded by a charge-coupled device cooled with liquid nitrogen, combined with monochromator. The excitation source was a monochromated xenon lamp. The spectra were corrected for the instruments response [10]. The PL spectra were acquired by exciting with a wavelength slightly shorter than the main absorption maxima of the compounds.

3. Results and discussion

3.1. General considerations

Depending on the nature of the components used (i.e., layered silicate and organic cation) and the preparation method, different types of hybrid can be obtained [7]. Phase-separated microcomposites (conventional composites) are obtained when the organic counterpart is unable to intercalate: silicate lamellae remain stacked in structures often referred to as tactoids as in the pristine mineral. Otherwise, when the organic cations penetrate in between the silicate layers, an intercalative system is obtained. In this case the composite shows, at least in principle, a well ordered multilayer morphology built up by alternating organic and inorganic layers. The most interesting and technologically promising materials are those belonging to this latter type, so that the understanding of the organic guest arrangement in between silicate lamellae is desirable, and XRD investigation is an irreplaceable technique to this aim.

In intercalated hybrids, the repetitive multilayer structure is well preserved, allowing the intra-layer spacing to be determined. Such an intercalation increases the intra-layer spacing with respect to the spacing of the pristine silicate, leading to a shift of the corresponding diffraction peak towards lower angle values. Moreover, the π-conjugated organic molecules accommodate within the lamellae and form peculiar ordered patterns, allowing for intermolecular interactions which can provide unique optical properties to the composites. Hence absorption and photoluminescence spectroscopy can be exploited as a complementary techniques to XRD analysis to give, beside the structural details about guest uptake in fluoromica layers, information on the intra-layer molecular arrangements as a function of both the dyes molecular species and their loading level.

The choice of **SME** fluoromica host, described by the formula $Na_{0.66}Mg_{2.68}(Si_{3.98}Al_{0.02})O_{10.02}F_{1.96}$, stems from its high aspect ratio ($L/W \cong 6000$, where L and W are length and thickness of silicate

platelets, respectively) low charge density, and small amounts of impurities [26].

Although **SME** crystal structure is unknown, Cs-fluoro hectorite [27] seems to be a reasonable approximation to it, even if the morphologic aspect of the former (large lamella-like) is significantly different from that of the latter (lath-like) [3]. To improve the similarity between Cs-fluoro hectorite and **SME**, the Cs^+ ion was replaced by Na^+, and *b*-axis of the unit cell was adapted to take into account the ionic radius contraction. This structure was adopted as the reference fluoromica for the interpretation of the diffraction data.

According to previous findings, the dry **SME** interlayer spacing [$d_{(001)}$] is close to 0.96 nm [28]. Any increase of this distance in a composite sample, detectable by XRD experiment, is a clear signature of an organic dye intercalation. However, the knowledge of the *d*-spacing in the vertical direction alone is not enough to completely evaluate the physical space occupied by the intercalated organic molecules, since it does not provide any insight into the other two horizontal dimensions. In addition, even if the intercalated molecules are packed together to yield ordered groups of molecules, the range of structural order achievable along the horizontal directions is insufficient to observe significant diffraction effects in an XRD pattern.

The loss of horizontal coherence in the packing of this kind of composite materials occurs when a size-mismatch takes place between the distances among the ions of the layered silicate directly involved in the interactions with the dyes, and the actual dimensions of the packed groups of intercalated molecules. Such dimensional mismatch is generally referred to as *incommensurability*.

In order to complement the partial information provided by XRD investigations, calculations in the framework of the well established space-filling model [29] were performed in order to: (i) explain the increase of the interplanar distance in the vertical direction, (ii) evaluate the extent of the horizontal occupation between the fluoromica layers by the packed molecules, and (iii) qualitatively estimate possible arrangements of the guest dyes.

The models of all the composites were built up by the MATSTUDIO package [30] and optimized to give the minimum overlap among atoms belonging to different molecules, compatibly with the maximum achievable packing, according to the spirit of the space-filling models.

To highlight the intercalated dye arrangement, the steric hindrance of the organic molecules has to be taken into account. While **Ox1**$^+$ molecular cation can be considered a planar rigid chromophore, and the **R6G**$^+$ one has only limited internal degree of freedom, the chemical structure of **TF**$^{2+}$ molecule (Scheme 1) allows the dye to assume a large variety of conformations, each one implying a different coverage of the **SME** *a*–*b* plane.

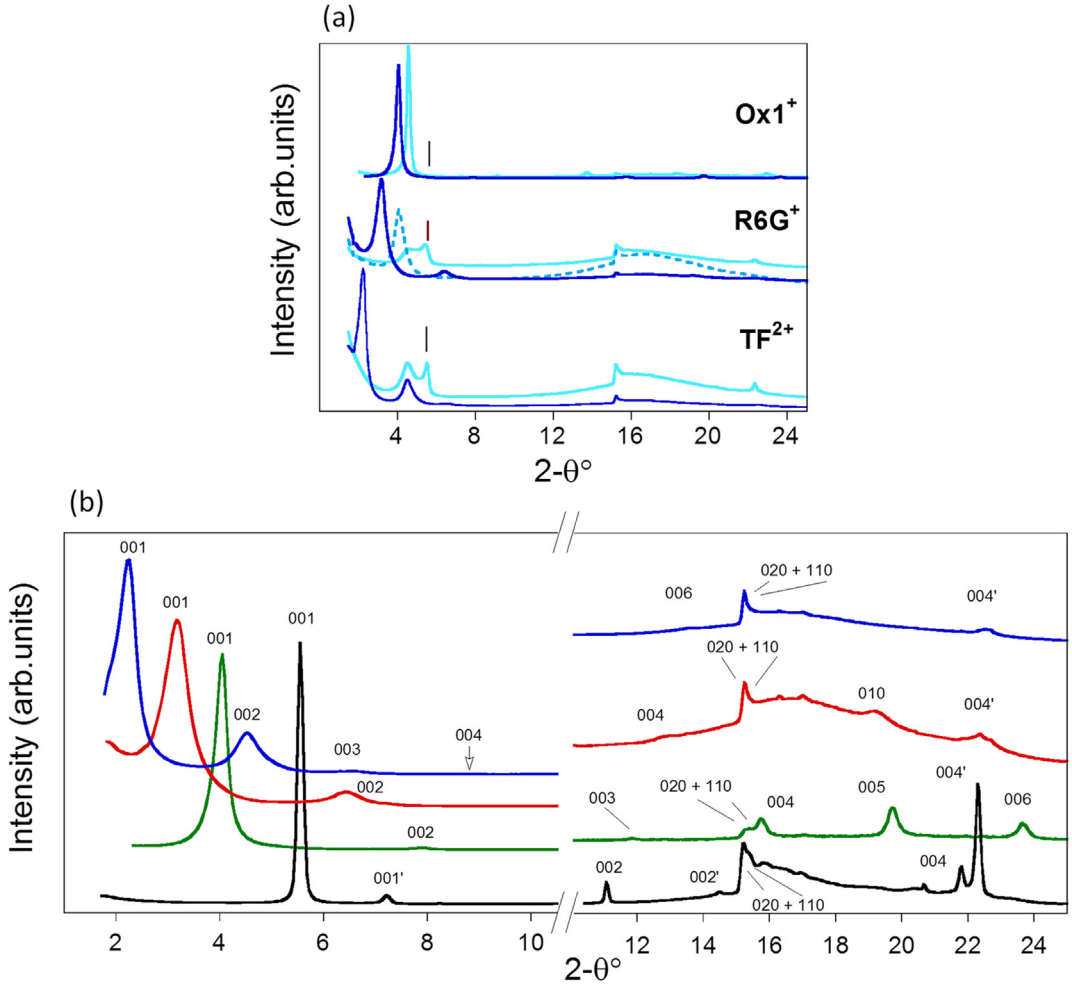

Fig. 1. a) Synchrotron XRD patterns of hybrids of **Ox1**$^+$, **R6G**$^+$, and **TF**$^{2+}$ derivative, at different loading amounts (blue line for the high-loading sample, azure line for low loading sample; dashed line for the intermediate loading of **R6G**$^+$). The vertical bars indicate **SME** (001) peak. b) Synchrotron XRD patterns of **SME** (black line) and largely loaded hybrids of **Ox1**$^+$ (green line), **R6G**$^+$ (red line), and **TF**$^{2+}$ (blue line), the (00*l*) reflections are indicated. Wavelength is 0.12 nm. The intensities are vertically shifted for clarity.

Table 1
Selected *d*-spacings (nm) of different samples as powders (see text).

Sample		Spacings[a]						
SME[b]		1.240′ **001**	*0.955″ 001*	0.620′ **002**	*0.472″ 002*	*0.316″ 003*	0.309′ **004**	0.248′ **005**
Ox1^{+}[c]	Low loading	1.52^{O} 001	*0.955″ 001*	0.755^{O} 002	0.503^{O} 003	0.376^{O} 004		
	High loading	1.740^{O} 001	0.868^{O} 002	0.580^{O} 003	0.437^{O} 004	0.350^{O} 005	0.291^{O} 006	
R6G^{+}	Low loading	1.700^{R} 001	*0.955″ 001*	0.424^{R} 002				
	High loading	2.140^{R} 001	1.070^{R} 002	0.705^{R} 003	0.532^{R} 004	0.424^{R} 005	0.360$^{\pi d}$	
TF^{2}$^{+}$	Low loading	1.520^{T} 001	1.240′ **001**	*0.955″ 001*	0.620′ 002	0.513^{T} 003		
	High loading	3.110^{T} 001	1.550^{T} 002	1.035^{T} 003	0.780^{T} 004	0.514^{T} 006		

[a] Corresponding (001) is indicated below, bold and italics characters are used for wet and dry **SME** respectively.
[b] Spacings related to wet **SME** are indicated with an apostrophe, while those related to dry **SME** are quoted in italic with double apostrophe.
[c] Peaks attributed to reflections belonging to the same crystallographic direction are indicated with O for **Ox1**$^{+}$, R for **R6G**$^{+}$, and T for **TF^{2}**$^{+}$ respectively (see text).
[d] This peak is attributed to **R6G**$^{+}$ π-stacking hence not indexed with the unit cell elsewhere considered (see text).

Beside the already mentioned incommensurability between the hybrid components, the dye loading achievable is limited by the silicate maximum cation exchange capacity (CEC) [14–17]. These two facts impose to assume quite different occupation factors for the inorganic/organic components in the calculation of the (*hkl*) intensity of the hybrids.

In the crystallographic view of intercalated hybrid materials, the dye aggregation in between the inorganic layers should be considered together with the effect of *c*-axis elongation. In this respect, the structural studies of bare fluoromica by Cattaneo et al. [31], and the studies about the intercalation of **R6G**$^{+}$ in taeniolite [32] showed the occurrence of a wide variety of peaks attributed to (00*l*) reflections. Other fine features of the XRD pattern, ascribed to the dye packing, contribute to shed light on the complexity of hybrid structure.

As will be detailed in the next section, the XRD patterns of all considered hybrids show pronounced variability both in spacing and intensity along with crystallographic direction [00*l*] as a function of loading. Contrariwise reflections observed in dry or wet **SME** and attributed to different [*h k l*], Fig. 1b, stay unchanged both in position and in intensity; this fact confirms that the two components of the hybrid contribute independently to the crystal diffraction.

Given the incommensurability between **SME** and any organic dye molecule, the dye aggregation is variable in the hybrid, as incomplete loading is achievable in all cases [14–17]. This fact originates an unregistered stacking in the basal clay plane, affecting also the trend of (00*l*) reflections and complicating the intensity calculations. For these reasons a full structural resolution is not easily achievable.

However, possible models of intercalated dye packing can be conceived using peaks attributed to [00*l*]. Besides to check crystallite dimensions and perfection XRD line-profile analysis is useful to assess the degree of ordered packing. To this end Hosemann para-crystal approach [33] was chosen dealing with the loss of long-range order typical of organic materials (see next paragraph for details).

To enlighten to some deeper extent the structure of these composites and to form any reliable model, an estimation of the effectively intercalated dye content is required. Hence we measured the amount of organic residue by thermogravimetric analysis and, after appropriate correction of the ratios due to different molecular weights, we obtained, for maximum loading, values of 0.18, 0.22, and 0.1 for **Ox1**$^{+}$, **R6G**$^{+}$, and **TF^{2}**$^{+}$ respectively [14–18]. This result evidences a molar ratio below one between fluoromica and dye, as largely expected in view of the hindrance of dye molecule inside the hybrid unit cell; therefore the contribution of fluoromica to the overall diffraction is prevailing in all cases. In order to give a reliable vision of aggregation in these complex systems, we resorted to compare the series of experimental [00*l*] peaks with calculated ones taking into account the contribution of **SME** only or **SME** + dye, packed in different situations, depicted by space filling molecular models. The previously mentioned occupation factors were employed to build up molecular models with MATERIAL STUDIO package [30]. A unit cell with elongated *c*-axis was chosen according to the diffraction data. The composite unit cell content was considered constituted by dye molecule and **SME** chemically unvaried after intercalation, as the substitution involves only a sodium ion.

In modeling calculations *P*1 space group was adopted, to account for the decrease in the hybrid crystal symmetry with respect to that of pure **SME**. The contribution of inorganic and organic part of the crystal to diffraction is however strongly affected by the mentioned unregistered stacking along *a*–*b* plane. The number of reflections available for structure factor calculations is rather small, being observable *d*-spacings below 0.28 nm, peaks which *d*-spacings are smaller than this value pertain only to the inorganic part.

The last two observations prevent therefore the use of either the recently appeared approach of Difference Envelope Density [19] or atomic pair distribution function analysis of X-ray powder diffraction data [20].

It is worth mentioning that also the combination of XRD data with ^{19}F NMR studies [21] cannot help because of both incommensurability between clay and dyes and possible multiple arrangement of the dye intra-layers.

3.2. XRD

The intercalation of the three different dyes inside **SME** intralayer space was monitored by powder XRD analysis. The measurements were performed at different wavelengths (energy ranged from 10.34 to 6.2 keV, i.e. $1.2 \leq \lambda \leq 2$ nm) in order to detail both long and short spacings.

Accurate *d*-spacing determination of both hybrid materials and pristine **SME** is reported in Table 1. Moreover the results of a complete full profile analysis in the Hosemann approximation along [00*l*] [34] calculated by means of the program package developed by Enzo et al. [35], are listed in Table 2.

Table 2
Line profile analysis of selected fluoromica hybrids as powders.

Sample	$L_{[001]}$[a]	ε_{rms}[b]	$g_{[001]}$[c] 100/200	$g_{[001]}$ 200/300	$g_{[001]}$ 300/400	$g_{[001]}$ 400/500	$g_{[001]}$ 500/600
SME	41	0.3	0.95	1.7			
SME wet	30	0.3	1.2	0.9			
Ox1^{+}	18.5	0.4	1.2	0.9	1.6	0.6	0.4
R6G^{+}	10	1.6	3.8	2.8	1.5	1.9	
TF^{2+}	11.5	1.6	5.7	3.8			2.3[d]

[a] L is the average crystallite dimension (nm) as derived from Ref. [35]. The estimated standard deviation (e.s.d.) is <1 nm.
[b] ε_{rms} is the non-uniform strain (%) which e.s.d. is 0.025.
[c] g_{hkl} is the lattice fluctuation factor (%) according to Hosemann paracrystal theory, calculated over closest order.
[d] In this case the referred reflections are (300) and (600).

In Fig. 1 XRD patterns of hybrids of **SME** and the three dyes **Ox1**$^{+}$, **R6G**$^{+}$, and **TF**$^{2+}$ as a function of loading level (a) and at maximum loading achievable (b), together with the reflection attribution, are shown. We take advantage of **SME** indexing reported in Refs. [27] and [31], and indicate the relevant (*hkl*) attribution following the sequence detailed in Table 1.

It should be mentioned that the **SME** is highly hydrophilic consequently the XRD spectra of the hybrids consist of peaks attributed to [00*l*] of dry fluoromica (indicated with a single apostrophe in both Table 1 and Fig. 1b), mixed with others pertaining to wet fluoromica (quoted with double apostrophe in the table). Other (*h k l*) reflections are common to both dry and wet material, so the indexing of relevant peaks is reported in Fig. 1b without any further distinction.

XRD spectra of bare dyes, reported in Figs. S1–S3 of Supplementary data, show no common peak with those of high loading hybrids (Fig. 1b). The largest *d*-spacings observed in the former cases are 1.41, 1.10, 4.20 nm for **Ox1**$^{+}$, **R6G**$^{+}$, **TF**$^{2+}$ respectively, while the largest one of the loaded **SME** samples is close to 1.24 nm (Table 1). This indicates that in all the samples, the amount of pristine dye salt external to the clay is lower than the XRD sensitivity (generally over 2%), and that most of the dye is intercalated in between **SME** lamellae.

Another feature of the XRD profiles of differently loaded hybrid samples consists in the progressive shift of the peaks – belonging to [00*l*] – as a function of the loading level, owing to the arrangement variability of the intercalated dyes. In fact largest *d*-spacing, starting from 1.24 nm (wet **SME**), increases to 1.74 nm, 2.14 nm and 3.11 nm for **Ox1**$^{+}$, **R6G**$^{+}$, and **TF**$^{2+}$ respectively (Table 1).

Moreover the peaks pertaining to pristine **SME**, visible in the spectra of the less loaded samples (vertical bars on (001)SME in Fig. 1a), are no longer present in the highly loaded samples as a consequence of the effective intercalation of all the available fluoromica. In the **Ox1**$^{+}$ case, the peak proper to the pristine **SME** is never observed independently of the amount of loading, because of both the presence of a small water residue, and a partial overlap with the hybrid (001) tail.

As previously mentioned, when the dye loading tends towards the maximum charge allowed by the CEC, no residual of **SME** [00*l*] can be measured, indicating that also in the condition of dye-**SME** ratio well below one, noticeable intra-layer size increment is achieved in **SME** lamellae, irrespectively of the residual water content. This shows that in these materials, considerable voids are present within the intercalated lamellae, as a consequence of the inability of the dyes to give rise to ordered groups of molecule on a very long range scale.

In all cases several orders of the same crystallographic direction, [001], are detected, indicating a pronounced coherence inside the intra-layer channels at high loading. In this respect profile analysis carried out along this direction (see Table 2) supplied significant parameters describing the order degree achieved in the hybrids: i) crystallite size L_{hkl}, ii) non-uniform strain ε_{rms}, (iii) lattice fluctuation factor g_{hkl} [34]. Specifically, the first maps the diffraction coherence, while the second and third ones describe the internal perfection, i.e. lower values indicate larger diffraction coherence inside a crystallite.

In Table 2 the ε_{rms} and g_{hkl} parameters of wet **SME** are found to be comparable in value to the corresponding ones of the hybrids, especially in the case of **Ox1**$^{+}$. This shows that the intercalated systems are characterized by well-formed and dimensionally regular crystallites, as in the case of pristine **SME**. Conversely the values appropriate to **TF**$^{2+}$ indicate more dimensional heterogeneity of the crystallites in the samples, possibly as a consequence of the greater internal flexibility of these intercalating molecules, which allows them to arrange in different ways in between the silicate layer.

Aside from wide elongation of *c*-axis, irrespectively of both the dye type and the loading level, a double peak at ~15.5° (2θ) attributable to (020) + (110) reflections of **SME**, is present in all the spectra. This is an indication that the dye intercalation does not appreciably perturb the periodicity along the horizontal dimensions, parallel to the *a*–*b* planes. This observation confirms that the **SME** and the dyes contribute quite independently to the diffraction, at least in the directions parallel to the lamella plane.

The values of the effective intra-layer size obtained from the *d*-spacings reported in Table 1 and derived by means of space-filling models are listed in Table 3. As expected in the cases of **Ox1**$^{+}$ and **R6G**$^{+}$ the *c*-axis elongation is coherently related to the loading: at low loading regimes the intercalated molecules can accommodate in a substantially flat way, while at high loadings the progressive standing up of the molecules related to the formation of packed groups of dyes, becomes evident from the extent of the *c*-axis elongation, which becomes more and more relevant.

A different situation is observed in **TF**$^{2+}$ case, where wide variability in *d*-spacings is observed as a function of loading level, since the octyl side-chains can assume quite various conformations, as detailed in the next section.

The tilt angle between the dye mean molecular axis and the fluoromica layer, indicated in column 4 of Table 3, has been calculated by using space-filling model with the aid of MATERIALS STUDIO package [30]. The maximum space effectively accessible to the molecules assumed in linear backbone conformation inside the **SME** intra-layer space was evaluated. Specifically, for **TF**$^{2+}$ case (Table 3) a range of values of tilt angle are reported, as a function of molecular conformations adopted by the intercalated dye.

In order to build up appropriate models of intra-layer arrangements of the dyes, we calculated the integrated intensity of [00*l*] reflections considering unit cell with expanded *c*-axis derived from modified F-hectorite [27] in the *P*1 approximation, as no higher symmetry can be conceived from XRD data. The intercalation of the dyes within the **SME** layers, taken in the conformation optimized by the COMPASS program of MATERIAL STUDIO package [30], was carried out adopting suitable orientations among those allowed by space-filling hindrance. The molecule position was finally varied by the rotation around the *c*-axis. The major constraint to be fulfilled was the experimental occupation factor of organic molecule which can vary upon the loading level.

As mentioned before, a *P*1 triclinic unit cell was adopted displaying following parameters: $a = 0.520$, $b = 0.909$ and $c = 0.960$ nm and $\alpha = \gamma = 90°$ and $\beta = 99.2°$. For any specific case *c*-axis was given the appropriate length (see Table 3).

A series of calculations have been performed to obtain the most favorable closest aggregations of the molecules into the intra-layer space and the most encouraging results are reported in Table 4. Of

Table 3
Evaluation of intra-layer space from *d*-spacings in different composites.

SAMPLE	$d_{(001)}$	Intra silicate layer space[a]	Dye/layer tilt angle (°)
SME	0.96	0.26[a]	–
Ox1^{+} (low loading)	1.51	0.40	0
Ox1^{+} (high loading)	1.74	0.62	20
R6G^{+} (low loading)	1.50	0.38	0
R6G^{+} (high loading)	2.12	1.01	50
TF^{2+} (low loading)	1.52	0.41	0
TF^{2+} (high loading)	3.1	1.98	10–40[b]

[a] Values are derived from CPK model optimized by MATERIALS STUDIO package (see text). For **SME** Na ionic radius is considered.
[b] In view of several conformations achievable by the molecule, a range of calculated angles is indicated (see text).

Table 4
Comparison of intensities of (00*l*) reflections of three cases differing in *a* axis length according to specific intercalated dye.[a]

(00*l*)	Dyes								
	Ox1^{+}			**R6G**$^{+}$			**TF**$^{2+}$		
	I_{obs}	I_{calc}	C_{SME}	I_{obs}	I_{calc}	C_{SME}	I_{obs}	I_{calc}	C_{SME}
(001)	100	100	100	100	100	100	100	100	100
(002)	1.60	2.07	2.31	5.50	4.50	1.50	26.60	22.20	9.19
(003)	0.33	0.66	0.61	0.49	0.55	0.40	0.90	0.50	0.34
(004)	1.60	0.80	0.70	0.20	0.03	0.01	0.14	0.15	0.07
(005)	2.68	2.61	0.90	0.12	0.20	0.19			
(006)	0.12	0.11	0.05				0.25	0.07	0.06

[a] Values are normalized to (001) and are multiplied by 10^2 to facilitate the comparison. The contribution to structure factors of dye intercalated in the **SME** intra-layer space is calculated using various occupation factors, whose values are derived from initial loading amount, TGA analysis, and molecular hindrance: 0.18, 0.22, and 0.10 for **Ox1**$^{+}$, **R6G**$^{+}$, and **T**$^{2+}$ respectively. C_{SME} indicates the contribution of **SME** only to the diffraction in the expanded unit cell (see text).

course taking into account the quite unfavorable ratio between experimental data and structural parameters to be determined, as well as to the difficulty in assessing water contribution to the diffraction, such a method must be considered a qualitative means to provide reasonable descriptions of these complex materials.

Nonetheless, some agreement in both the absolute values and trends between observed (I_{obs}) and calculated (I_{calc}) intensities can be recognized by comparing columns 1 and 2 for each dye in Table 4.

Even though the strong reduction of peak intensity after second order reflections implies an increasing uncertainty in the integrated intensity evaluation, the trends are still preserved. Moreover the agreement between the I_{obs} with those calculated as the contribution of the **SME** alone in the expanded unit cell (C_{SME}) is worse than those calculated accounting for both the contribution of **SME** and dye. These evidences constitute a clear indication that the approach supplies models capable to capture the general structural features of these complex systems, at least at a coarse grain level.

The different dye arrangements in between **SME** layers are described in the next section separately, and the CPK models are commented.

3.3. Packing models

In view of the lack of information on *a*–*b* plane packing arrangements and also of the values of dye occupation factors – less than unity as specified Section 3.1 – some stakes must be fixed in order to supply a reliable vision of the dye organization inside the enlarged **SME** layers.

Specifically the area of the closest achievable packing of the dye molecules should not exceed the maximum layer charge area value of **SME** (0.77 nm^2) [36], to preserve charge equilibrium. At the same time, the ratio between the area occupied by the dye, properly scaled by the real occupation factor, and the area of **SME** *a*–*b* plane – in the following indicated as filling ratio (FR) – has to model spatially heterogeneous samples, containing both closely packed molecules and void areas.

As mentioned above, the lack of (00*l*) **SME** peaks and the appearance of corresponding peaks at lower diffraction angles – i.e. larger *d*-spacings – in XRD spectrum of highly intercalated hybrids indicate the ubiquitous presence of intra-layer space expansion.

As a counter check, the comparison of the number of non-substituted unit cells versus that of the intercalated ones, coming from the model, was performed by selecting the most promising models in terms of both available interlayer space and intensity trend of [00*l*] calculated intensities. Reliable arrangements, assuming closest packing, are proposed in the following for each specific case.

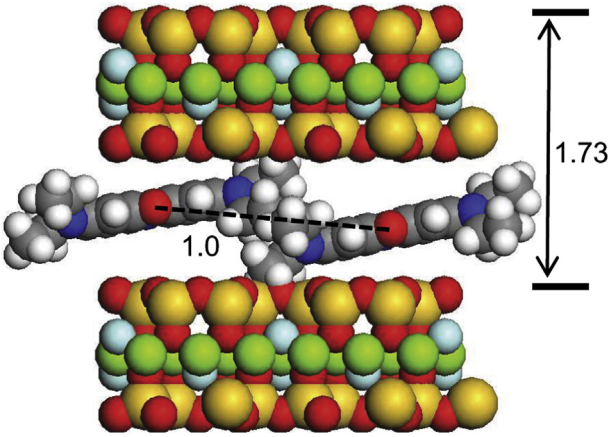

Fig. 2. Space-filling model of a composite of **SME** and **Ox1**$^{+}$ at high loading, as viewed along the channels. The distance between adjacent silicate layers and between close dye molecules is in nm. Different elements are indicated by yellow (Si), red (O), green (Mg), azure (F), gray (C), blue (N), and white (H) respectively.

3.3.1. $Ox1^+$

The oxazine-1 is a conjugated dye with a planar conformation readily intercalated into **SME** layers [8], in fact highly loaded hybrids display (001) spacing close to 1.74 nm along with five higher orders; the corresponding space filling model is shown in Fig. 2, where the oxygen atoms of two **Ox1**$^+$ molecules are separated by ~1 nm. In the spectrum region typical of dye molecule π-stacking (0.4 nm) no diffraction effect over background is observed. Moreover the calculated occupation factor, close to 0.18, is the maximum loading with respect to the CEC in spite of the large amount of not substituted **SME** regions. Molecular models with paired molecules at ~0.65 nm allow for two different dimer aggregation, namely with either faced or opposite diethyl amine groups. The bent shape of **Ox1**$^+$ molecule makes the opposite situation largely preferred to ensure the closest packing, as shown in Fig. 3, where an ordered 2D packing inside the silicate intra-layer space is depicted. Such an arrangement is constituted by four molecules, forming a quasi rectangular ensemble, realizing the closest packing, as viewed normally to the *a*–*b* **SME** plane in Fig. 3. This model yields an area value of about 0.8 nm^2, comparable with the average layer charge area (0.77 nm^2) [36].

An approximate calculation of the above defined FR gives a values close to 0.31, meaning that on 100 **SME** unit cells about 67 are not intercalated.

3.3.2. $R6G^+$

Rhodamine 6G is widely used for its relevant emitting properties and has been successfully intercalated in **SME** [17]. From XRD data four orders of [001] direction, $d = 2.14$ nm, are visible; more interestingly a new peak (0.36 nm) appears, attributable to the π-stacking of adjacent molecules, whose extension approaches 7 molecules, evaluated by using line profile analysis [35]. Noticeably, in the XRD spectrum of pure **R6G**$^+$ reported in Fig. S2 of Supplementary data, no spacing at 0.36 nm is registered, indicating that a peculiar close arrangement of the molecules in between the **SME** layers takes place when **R6G**$^+$ is intercalated. This crystallographic evidence readily accounts for a possible aggregation of the intercalated dye as coming out from PL experiments [17] (Section 3.4), in contrast with J-aggregate formation recently observed in 9-phenylanthracenyl rhodamine derivative [37].

In the case of high loading reliable space-filling models evidence **SME** intra-layer arrangement, constituted by a sequence of intercalated molecules, shown in Fig. 4. As proposed for **Ox1**$^+$ hybrids, also in this case the intra-layer molecular organization can be represented as a close packing of **R6G**$^+$, along the basal fluoromica plane, coherently with XRD outputs. The minimum distance achievable between two close sequences of adjacent π-stacked **R6G**$^+$ molecules, evaluated near to 1.4 nm, and the angle formed by mean molecular axis and silicate layer, calculated near to 50°, were considered. From these molecular arrangements, the closest packing achievable in case of high loading can be derived, namely a

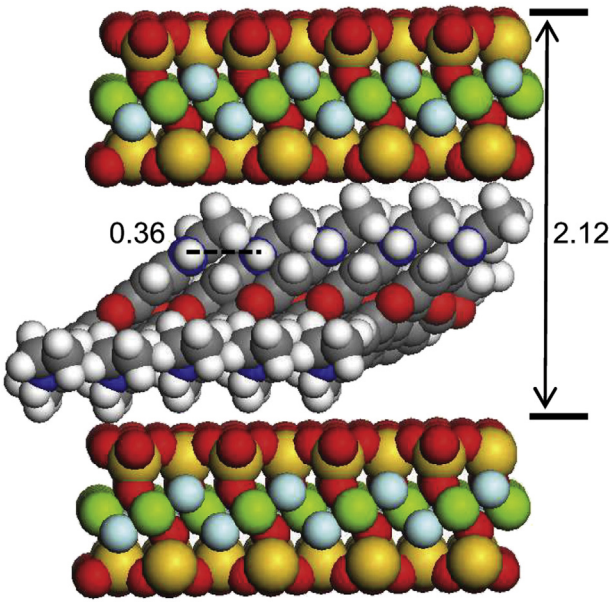

Fig. 4. Space-filling model of hybrid of **SME** and **R6G**$^+$ at high loading level, as viewed laterally to evidence π-stacking of the dye molecules. The distance between adjacent silicate layers and between close dye molecules is in nm.

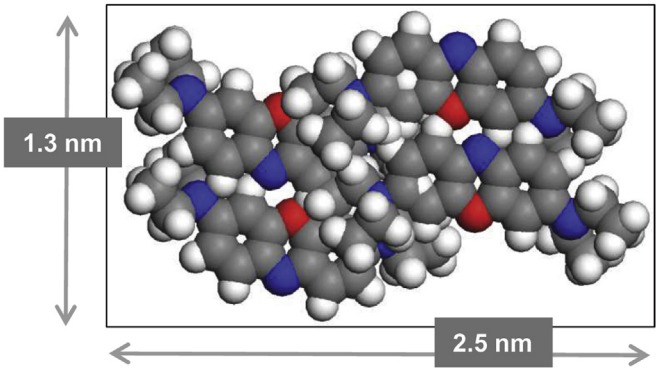

Fig. 3. Space-filling model of the closest packing of four **Ox1**$^+$ molecules, as viewed normally to the clay plane. The aggregate is placed inside the highly loaded **SME** composite. The atoms belonging to the silicate are omitted for the sake of clarity.

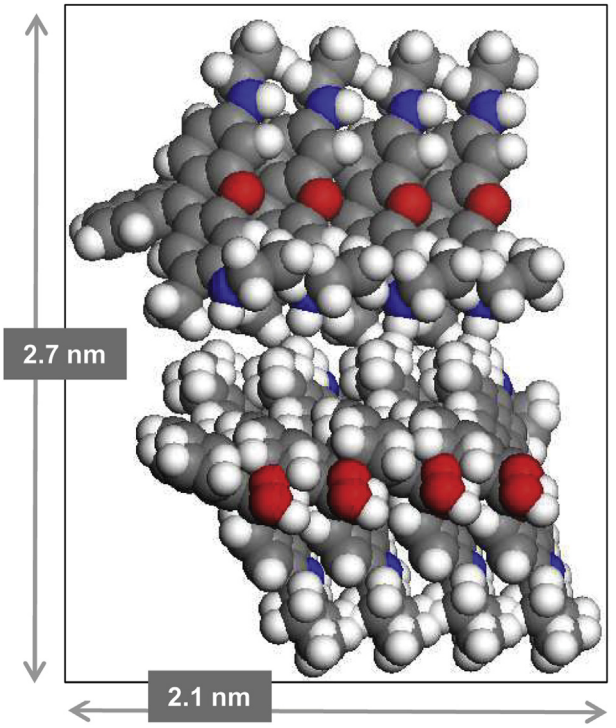

Fig. 5. Space-filling model of two antiparallel stacks of **R6G**$^+$, each formed by four molecules, closely packed inside the highly loaded composite. The arrangement is viewed along *c*-axis. The atoms belonging to the silicate are omitted for the sake of clarity.

model of antiparallel strips of π-stacked molecules can be conceived.

As exemplified in Fig. 5, the smallest area occupied by two strips, each one constituted by 4 molecules (the minimum number to guarantee a coherent packing) is close to 0.71 nm^2, a value compatible with the average layer charge area of **SME** (0.77 nm^2) [36]. It is worth mentioning that even considering parallel strips of π-stacked molecules, the derived area is about 0.8 nm^2, which supports the model credibility.

In this case FR ratio (0.33) is quite comparable to the **Ox1**$^+$ value in spite of the observed π-stacking of adjacent molecules; this observation can be justified by molecular size increase. Correspondingly, on 100 **SME** unit cells about 65 should be not intercalated.

3.3.3. TF^{2+}

Dialkyl-fluorene trimer with tethered quaternary ammonium groups was successfully intercalated in **SME** [16], and according to an increasing dye loading, different arrangements of the molecules could be inferred: at low CEC ratio, a flat molecular conformation was conceived in order to account for the experimental inter-layer spacing. At high loadings, where quite large spacings were found from XRD spectra, expanded molecular arrangements were more appropriate to explain the experimental data.

The molecule length in extended conformation (2.75 nm) matches the long spacing exceeding 3.1 nm in films and powders [14], while the dimension of the lateral chains only allows for molecular aggregation that exceeds 1 nm, due to the pendent octylic ammonium chains. These dimensional features explain the absence of a peak attributable to the π-stacking (0.4 nm) in the XRD spectra, instead observed in the case of **R6G**$^+$.

The feasibility of such different molecular arrangements within the silicate are granted by the great flexibility that the octyl side chains provide to this particular dye, as already observed in poly(9,9-(di-*n*,*n*-octyl)fluorene)s with different molecular weights [38,39]. Moreover such conformational changes require an energy cost [40] quite comparable with that calculated for clay layer expansion [41]. The complexity of the present system allows the octyl ammonium chains to accommodate either in flat conformation (0.41 nm channel thickness) at low loading or in an extended conformation (about 2 nm channel thickness) at high loading, as shown in Table 3.

Also in this case more than four orders of [001] direction are expressed in the spectrum. In this context the proposal of a unique model is clearly unfeasible, hence in Fig. S4 of Supplementary data just one possible model, supplying the intensity calculations reported in Table 4 – as viewed along [110] – is proposed. Among the calculated models compatible with both d-spacing and observed peaks attributed to [001] direction (see Table 3), the one displayed in Fig. S4 exhibits a small angle between mean molecular axis of **TF**$^{2+}$ and **SME** *a*–*b* plane. However in Table 3 a range of angles derived from different likely models is indicated.

Unlike the previous cases, no unique model of lateral packing can be proposed, because of both multiple conformations of octyl ammonium chains and the consequent orientations inside the large layers of **SME** lamellae.

Nevertheless a tentative FR value is derived of about 0.62, the highest in the series in view of molecule size; in this case the number of not intercalated unit cells does not exceed 37 on the average.

3.4. Optical characterization

SME hybrids loaded with the three fluorescent dyes are insoluble, hence the optical characterization (UV–vis absorption and PL spectra) was performed on the crystalline powders ground in KBr pellets. While absorption spectra are only slightly affected by the loading levels of the three dyes in the **SME**, the PL ones show huge differences with a color tunability upon **Ox1**$^+$ and mainly **R6G**$^+$ loading ratios. To better display the color changes in hybrid emission, the Commission Internationale de l'Éclairage (CIE) chromaticity diagram, which represents the mapping of human color perception in terms of two CIE parameters (*x*; *y*), is used (Fig. 6).

The absorption band of high and low loadings **Ox1**$^+$ hybrids pellets are broad, centered at 671 nm, slightly red-shifted with respect to the isolated **Ox1**$^+$ molecule, with a second peak at 613 nm, more intense for high loading, consistent with an excitonic band formation (*H*-dimers) [14]. In PL spectra, where isolated **Ox1**$^+$ molecules emission can be discriminated thanks to its higher PL quantum yield with respect to aggregate form, the peak at 672 nm indicates the presence of **Ox1**$^+$ isolated molecules in both lowly and highly loaded hybrids. Besides, a large red-shifted emission band at about 750–850 nm, dominant in the highly loaded sample, is present. As reported earlier, grain boundaries emission of large-size **Ox1**$^+$ aggregates adsorbed on the **SME**-edge-surface, hence not affecting interlamellar fluoromica spacing [14], are responsible of such a near infrared emission and contribute to the high energy peak observed in absorption spectra. The CIE coordinates of **Ox1**$^+$ hybrids slightly shift from (0.73; 0.26) to (0.72; 0.28) upon increasing dye content.

Both absorption spectra of **R6G**$^+$-based compounds show a broad band centered at 540 nm and a high energy shoulder at about 500 nm. On the contrary, huge differences in the emission spectra are observed in different loaded hybrids. Clear peaks at 555, 602, and 680 nm indicate contemporary contribution of **R6G**$^+$ isolated and aggregated phases for low dye loading. The intensity of the aggregated emission is dominant in the highly loaded compound. Differently from the **Ox1**$^+$ hybrids, the reiterated solvent extraction does not affect low energy emission intensity, thus indicating that the aggregated **R6G**$^+$ molecules are most probably confined in between lamellar planes. These results correlate well to the structural characterization and the model where a close packing of **R6G**$^+$ molecules is highlighted. Upon dye packing, the emission color can be tuned with a large change in CIE coordinated from orange (0.50; 0.48) to red (0.63; 0.35) for the low and high loading hybrids respectively.

The optical properties of **TF**$^{2+}$ hybrids are substantially identical: no aggregation can be envisaged and a main absorption band centered at 370 nm and a peak emission at 420 nm are observed. The lack in both hybrids of the high energy emission peak observed in the neat **TF**$^{2+}$ diluted solution [42] might be ascribable an increased planarity of the fluorene backbone or to inner filter effect (self-absorption) because of relatively high concentrations of intercalated fluorophore. No clear changes are observed in the low-energy tail of the PL hence an isolated phase of **TF**$^{2+}$ dyes can be envisaged with CIE coordinates (0.17; 0.09).

4. Conclusions

Hybrid composites constituted by fluoromica (**SME**) and π-conjugated molecules were prepared and studied by both XRD techniques and optical investigations (absorption and luminescence). The combination of the above characterizations with molecular modeling allowed us to unveil details on different packing arrangements which in turn affect the optical properties. Specifically, calculated [00l] intensities were compared with experimental ones in all considered cases and a significant trend was recognized, although a quantitative approach was prevented because of the unregistered stacking between dye and silicate along with the lamellae layers.

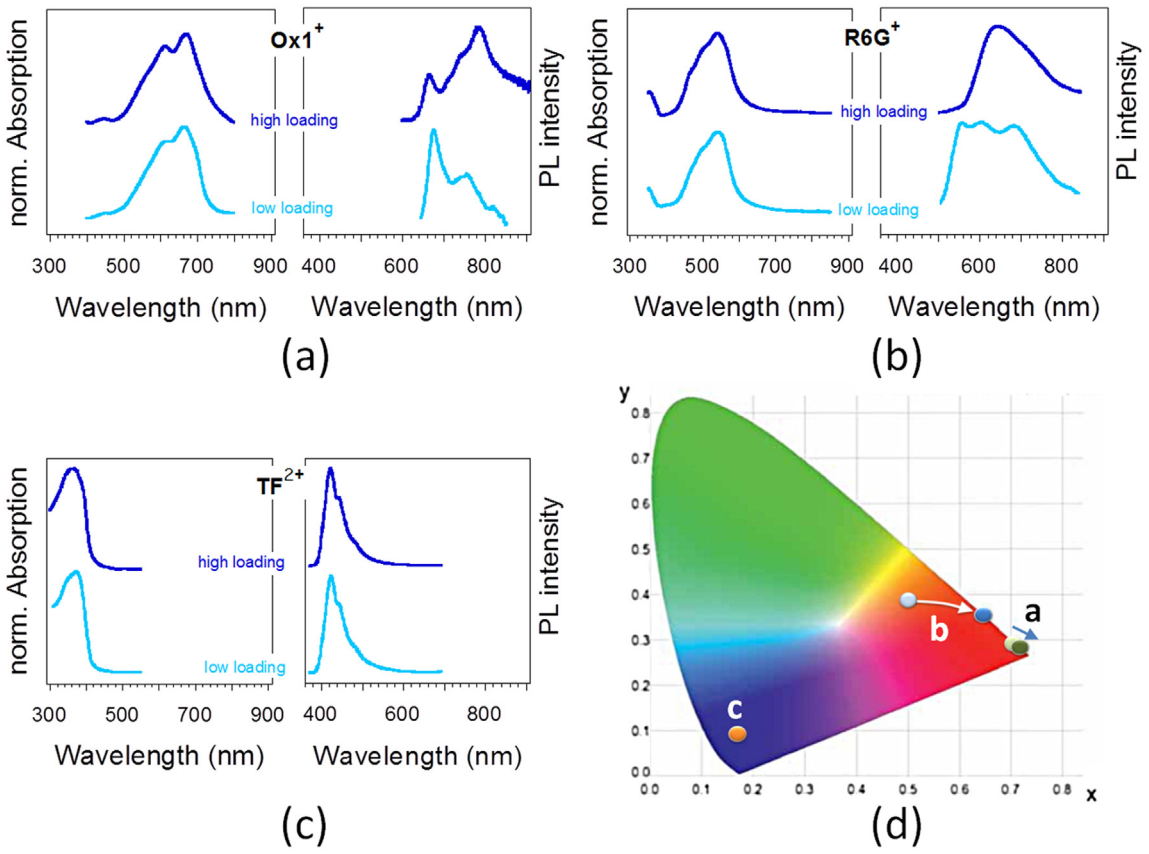

Fig. 6. UV–vis absorption and PL spectra of high (dark blue) and low loadings (light blue) hybrids in KBr pellets: **Ox1**$^{+}$ (a), **R6G**$^{+}$ (b), **TF**$^{2+}$ (c); spectra are vertically shifted for clarity. The CIE chromaticity diagram for hybrids emissions is reported (d).

Possible packing models were inferred, on this basis, accomplishing both **SME** CEC and occupation factors. According to the loading level, significant differences in optical features, especially in PL spectra, were observed.

In particular for **R6G**$^{+}$ case, which displays an impressive PL change, the correlation with molecule π-stacking is fully explanatory. While in other cases more limited variation occurred consistently with the lack of any π-stacking.

All in all the intra-layer insertion of a different dye at various loadings determines the packing type, pivoting the optical properties.

Acknowledgments

Thanks are due to Dr. G. Ricci and Dr. C. Botta for helpful discussions.

Appendix A. Supplementary data

Supplementary data related to this article can be found at http://dx.doi.org/10.1016/j.dyepig.2015.09.003.

References

[1] Ruiz-Hitzky E, Aranda P, Darder M, Ogawa M. Hybrid and biohybrid silicate based materials: molecular vs. block-assembling bottom-up processes. Chem Soc Rev 2011;40(2):801–28.
[2] Sanchez C, Julian B, Belleville P, Popall M. Applications of hybrid organic–inorganic nanocomposites. J Mater Chem 2005;15(35–36):3559–92.
[3] Sanchez C, Boissiere C, Cassaignon S, Chaneac C, Durupthy O, Faustini M, et al. Molecular engineering of functional inorganic and hybrid materials. Chem Mater 2014;26(1):221–38.
[4] Sanchez C, Lebeau B, Chaput F, Boilot JP. Optical properties of functional hybrid organic–inorganic nanocomposites. Adv Mater 2003;15(23):1969–94.
[5] Bailey L, Lekkerkerker HNW, Maitland GC. Smectite clay – inorganic nanoparticle mixed suspensions: phase behaviour and rheology. Soft Matter 2015;11(2):222–36.
[6] Park JH, Lim YT, Park OO, Kim JK, Yu JW, Kim YC. Stabilized blue emission from polymer–dielectric nanolayer nanocomposites. Adv Funct Mater 2004;14(4):377–82.
[7] Leone G, Ricci G. Layered materials chemistry: techniques to tailor new enabling organic-inorganic materials. In: Brunet E, Colón JL, Clearfield A, editors. Photofunctional Polymer/layered silicate hybrids by intercalation and polymerization chemistry; 2015.
[8] Yang PD, Wirnsberger G, Huang HC, Cordero SR, McGehee MD, Scott B, et al. Mirrorless lasing from mesostructured waveguides patterned by soft lithography. Science 2000;287(5452):465–7.
[9] Shen Y, Swiatkiewicz J, Prasad PN, Vaia RA. Hybrid near-field optical memory and photofabrication in dye-doped polymer film. Opt Commun 2001;200(1–6):9–13.
[10] Moreau J, Giovanella U, Bombenger JP, Porzio W, Vohra V, Spadacini L, et al. Highly emissive nanostructured thin films of organic host–guests for energy conversion. ChemPhysChem 2009;10(4):647–53.
[11] Meinershagen JL, Bein T. Optical sensing in nanopores. Encapsulation of the solvatochromic dye Nile red in zeolites. J Am Chem Soc 1999;121(2):448–9.
[12] Lee TW, Park OO, Yoon JH, Kim JJ. Polymer-layered silicate nanocomposite light-emitting devices. Adv Mater 2001;13(3):211–3.
[13] Utracki LA, Broughton B, Gonzalez-Rojano N, de Carvalho LH, Achete CA. Clays for polymeric nanocomposites. Polym Eng Sci 2011;51(3):559–72.
[14] Leone G, Giovanella U, Porzio W, Botta C, Ricci G. In situ synthesis of fluorescent poly(norbornene)/oxazine-1 dye loaded fluoromica hybrids: supramolecular control over dye arrangement. J Mater Chem 2011;21(34):12901–9.
[15] Giovanella U, Leone G, Ricci G, Virgili T, Lopez IS, Rajendran SK, et al. Oxazine-1 J-aggregates in polymer nanohybrids. Phys Chem Chem Phys 2012;14(39):13646–50.

[16] Leone G, Giovanella U, Bertini F, Hoseinkhani S, Porzio W, Ricci G, et al. Hierarchically structured, blue-emitting polymer hybrids through surface-initiated nitroxide-mediated polymerization and water templated assembly. J Mater Chem C 2013;1(40):6585–93.
[17] Leone G, Giovanella U, Bertini F, Porzio W, Meinardi F, Botta C, et al. Poly(-styrene)-graft-/rhodamine 6G-fluoromica hybrids: synthesis, characterization and photophysical properties. J Mater Chem C 2013;1(7):1450–60.
[18] Giovanella U, Leone G, Galeotti F, Mróz W, Meinardi F, Botta C. FRET-assisted deep-blue electroluminescence in intercalated polymer hybrids. Chem Mater 2014;26(15):4572–8.
[19] Yakovenko AA, Wei ZW, Wriedt M, Li JR, Halder GJ, Zhou HC. Study of guest molecules in metal organic frameworks by powder X-ray diffraction: analysis of difference envelope density. Cryst Growth Des 2014;14(11):5397–407.
[20] Demal J, Hynek J, Kovar P, Dai Y, Taviot-Gueho C, Demel O, et al. Insight into the structure of layered zinc hydroxide salts intercalated with dodecyl sulfate anions. J Phys Chem C 2014;118(46):27131–41.
[21] Cadars S, Allix M, Brouwer DH, Shayib R, Suchomel M, Garaga MN, et al. Long- and short-range constraints for the structure determination of layered silicates with stacking disorder. Chem Mater 2014;26(24):6994–7008.
[22] Rivnay J, Noriega R, Kline RJ, Salleo A, Toney MF. Quantitative analysis of lattice disorder and crystallite size in organic semiconductor thin films. Phys Rev B 2011;84:045203 (1–20).
[23] Gozzo F, De Caro L, Giannini C, Guagliardi A, Schmitt B, Prodi A. The instrumental resolution function of synchrotron radiation powder diffractometers in the presence of focusing optics. J Appl Crystallogr 2006;39:347–57.
[24] Hammersley AP, Svensson SO, Hanfland M, Fitch AN, Hausermann D. Two-dimensional detector software: from real detector to idealised image or two-theta scan. High Press Res 1996;14:235–48.
[25] Roisnel T, Rodriguez-Carvajal J. WinPLOTR: a windows tool for powder diffraction pattern analysis. Mater Sci Forum 2001;378–381:118–23.
[26] Miwa Y, Drews AR, Schlick S. Detection of the direct effect of clay on polymer dynamics: the case of spin-labeled poly(methyl acrylate)/clay nanocomposites studied by ESR, XRD, and DSC. Macromolecules 2006;39:3304–11.
[27] Breu J, Seidl W, Stoll A. Fehlordnung bei Smectiten in Abhängigkeit vom Zwischenschichtkation. Z Anorg Allg Chem 2003;629:503–15.
[28] Tateyama H, Nishimura S, Tsunematsu K, Jinnai K, Adachi Y, Kimura M. Synthesis of expandable fluorine mica from talc. Clays Clay Miner 1992;40:180–5.
[29] Corey RB, Pauling L. Molecular models of amino acids, peptides, and proteins. Rev Sci Instrum 1953;24:621–7.
[30] MATSTUDIO modeling release 4.0. 9685 Scranton Rd., San Diego, CA, USA: Accelrys Inc.; 2003. www.accelrys.com.
[31] Cattaneo AS, Bracco S, Comotti A, Galimberti M, Sozzani P, Eckert H. Structural characterization of pristine and modified fluoromica using multinuclear solid-state NMR. J Phys Chem C 2011;115:12517–29.
[32] Sasai R, Fujita T, Iyi N, Itoh H, Takagi K. Aggregated structures of rhodamine 6G intercalated in a fluor-taeniolite thin film. Langmuir 2002;18:6578–83.
[33] Hindeleh AM, Hosemann R. Microparacrystals – the intermediate stage between crystalline and amorphous. J Mater Sci 1991;19:5127–36 [and ref. therein].
[34] Following Hosemann paracrystal model [33] expressed by L_{hkl} – crystallite size, lattice fluctuation factor $g_{(hkl)} = (\overline{d^2}_{(hkl)}/\overline{d}^2_{(hkl)} - 1)^{1/2}$, indicating the standard deviation of $d_{(hkl)}$ evaluated over more orders of crystallographic directions, and non-uniform strain $\varepsilon_{\mathrm{rms}} = (\langle e^2 \rangle)^{1/2}$, where $e = \delta d_{(hkl)}/d_{(hkl)}$, defined as root mean square of the lattice variations in the sample.
[35] Enzo S, Fagherazzi G, Benedetti A, Polizzi S. A profile-fitting procedure for analysis of broadened X-ray-diffraction peaks. 1. Methodology. J Appl Crystallogr 1988;21:536–40.
[36] Yang JH, Han YS, Choy JH, Tateyama H. Intercalation of alkylammonium cations into expandable fluorine mica and its application for the evaluation of heterogeneous charge distribution. J Mater Chem 2001;11:1305–12.
[37] Kim S, Fujitsuka M, Tohnai N, Tachikawa T, Hisaki I, Miyata M, et al. Unprecedented J-aggregate formation of rhodamine induced by 9-phenylanthracenyl substitution. Chem Commun 2015;51:11580–3.
[38] Grell M, Bradley DDC, Ungar G, Hill J, Whitehead KS. Interplay of physical structure and photophysics for a liquid crystalline polyfluorene. Macromolecules 1999;32:5810–7.
[39] Brinkmann M. Directional epitaxial crystallization and tentative crystal structure of poly(9,9′-di-*n*-octyl-2,7-fluorene). Macromolecules 2007;40:7532–41.
[40] Winokur MJ, Slinker J, Huber DL. Structure, photophysics, and the order–disorder transition to the β-phase in poly(9,9-(di-*n*,*n*-octyl)fluorene). Phys Rev B 2003;67:1–11. 184106.
[41] Whitley HD, Smith DE. Free energy, energy, and entropy of swelling in Cs-, Na-, and Sr-montmorillonite clays. J Chem Phys 2004;120:5387–95.
[42] Leone G, Galeotti F, Porzio W, Scavia G, Barba L, Arrighetti G, et al. Poly(-styrene)/oligo(fluorene)-intercalated fluoromica hybrids: synthesis, characterization and self-assembly. Belstein J Nanotechnol 2014;5:2450–8.